Chiral couplings of W' and top quark polarization at the LHC

Shrihari Gopalakrishna,[1,2] Tao Han,[3] Ian Lewis,[3] Zong-guo Si,[4] and Yu-Feng Zhou[5]

[1]*The Institute of Mathematical Sciences, Chennai 600113, India*
[2]*School of Physics, University of Melbourne, Victoria 3010, Australia*
[3]*Department of Physics, University of Wisconsin, Madison, Wisconsin 53706, USA*
[4]*Department of Physics, Shandong University, Jinan Shandong 250100, China*
[5]*Kavli Institute for Theoretical Physics China, Institute of Theoretical Physics,
and Key Laboratory of Frontiers in Theoretical Physics, Chinese Academy of Sciences, Beijing, 100190, China*

If a TeV-scale charged gauge boson (W') is discovered at the Large Hadron Collider (LHC), it will become imperative to determine its chiral couplings to standard model (SM) fermions in order to learn about the underlying theory containing the W'. We describe the reconstruction of the tb decay mode of the W' at the LHC, and identify various kinematic observables such as the angular distributions of the top quark and the lepton resulting from top decay that can be used to disentangle the chiral couplings of the W' to SM fermions. We demonstrate by presenting analytical expressions, numerical simulations, as well as intuitive illustrations for these observables at the LHC that among the SM fermions, the polarized top quark can most directly probe the chirality of such couplings.

I. INTRODUCTION

New heavy gauge bosons appear in many gauge-sector extensions of the standard model (SM). The Large Hadron Collider (LHC) has the potential to discover such vector states [1,2] if their masses are not much larger than a few TeV and their couplings to standard model states are not too suppressed. Once the discovery of a new heavy state becomes established at the LHC, one would turn next to measuring its properties, such as mass, spin, and couplings. Kinematical observables such as the invariant-mass or transverse momentum distributions of its decay products can be used to extract its mass, angular distributions of its production and decay products can be exploited to confirm its spin, and measured event-rates in various channels can fix combinations of its coupling strengths to the SM fields. Another critically important property is the chirality of the new state's couplings to SM fermions. Knowing the fermionic chiral couplings can help us glean insight into the structure of the new gauge theory and possibly its gauge-symmetry breaking. A prominent example is the left-right symmetric theory with spontaneous parity violation [3], in which a new heavy charged gauge boson couples to the SM fermions with right-handed chirality.

If the branching fractions (BR) decaying to the SM leptons are not particularly suppressed, the leptonic decays of the new heavy vector state are the much studied "golden modes." The chiral nature of the couplings of a neutral vector boson (generically denoted by Z') can be probed via the charge forward-backward asymmetry ($A_{\rm FB}$) [4]. This is unavailable at hadron colliders, however, for a charged vector boson (generically denoted by W'). This follows from an important fact due to the spin correlation for chiral couplings, that for the two-body leptonic decays $q\bar{q}' \to W'^{-(+)} \to \ell^{-(+)}\nu$, the charged lepton ℓ^- (antilepton ℓ^+)

moves favorably in the direction of the initial quark q (antiquark q') direction, regardless of the pure left-handed (L) or right-handed (R) coupling of the W'. However, Ref. [5] shows that $pp \to W'W$ production and $W' \to W\ell^+\ell^-$ decay can distinguish the pure left-handed versus pure right-handed cases. Although leptonic channels are experimentally clean and will thus be among the first to be observed, much information about the heavy vector boson chiral couplings can be learned by analyzing the spin correlations of longer decay chains. Also, if the leptonic branching fractions are suppressed in a given new-physics scenario (common in warped extra dimension models [6,7] for instance), one will be forced into analyzing more complicated final states including, for instance, top quarks.

In this paper, we study in detail the process

$$pp \to W' \to t\bar{b} \to \ell^+ \nu b\bar{b}, \qquad (\ell = e, \mu) \qquad (1)$$

and wish to determine the W' chiral couplings by making use of various kinematical variables. The motivations for this proposal are many: First, the observation of such a charged gauge boson W' would not only unambiguously imply a symmetry beyond a simple $U(1)$ for a Z', which could be very common in a variety of scenarios but inconclusive about its origin, but also most likely predict the existence of a Z' in the same gauge multiplet. Second, in some new-physics models, there are strongly interacting neutral resonances (such as a Kaluza-Klein (KK) gluon) fairly close in mass to the Z's. These resonances would decay to $t\bar{t}$ with much larger rates, masking the electroweak neutral gauge boson and causing it to be difficult to stand out in the $t\bar{t}$ channel [8]. The mode $W' \to tb$ final state, on the other hand, would be, in principle, free from this problem. Third, a W' typically leads to a sizable

production rate and larger decay branching fraction to the top, with a slightly more favorable phase space. (See also Ref. [9] for the $W' \to tb$ cross section.) Finally, as we will demonstrate later, the angular distribution of the lepton reconstructed in the top-quark rest frame serves as a diagnostic of the top spin which in turn contains information on the chirality of the W' coupling. This point above was first considered in [10]. We stress that this feature is unique for the top-quark final state, and unavailable to any other W' decay modes to SM particles.

We will utilize techniques that determine the quark direction on a statistical basis. We will discuss issues in the reconstruction of the top quark and how detector resolution and SM backgrounds affect the determination of the W' chirality. The discussion will be kept model independent, as long as the W' branching fraction to $t\bar{b}$ is not too small and that the top-quark decays are essentially as in the SM. This assumption is not particularly restrictive since it has been shown [11] that the lepton angular distribution from top decay is insensitive to the presence of small anomalous tbW couplings.

The paper is organized as follows: In Sec. II, we specify a model-independent theoretical framework defining the W' chiral couplings to SM fields and list the constraints on W' bosons from current experiments. In Sec. III, we discuss techniques to reconstruct the event for the $W' \to tb$ decay mode at the LHC. In Sec. IV, we present a detailed exposition of ways to determine the chiral couplings of the W' at the LHC using many complementary measurements, namely: (i) the angular distribution of the top quark; (ii) the angular distribution of the lepton in the top rest frame with respect to the top moving direction; (iii) the lepton transverse momentum distribution; (iv) the angular distribution of the lepton in the W rest frame with respect to the W moving direction. We end with discussions and conclusions in Sec. V. The analytical expression for the angular distribution of the lepton in the top-quark rest frame is fully worked out in Appendix A, and the technical details of evaluating a contour integral encountered there is given in Appendix B.

II. THEORETICAL FRAMEWORK

Many beyond the SM theories contain new heavy charged vector bosons that couple to the SM. For example, a left-right symmetric theory [3] has a charged gauge boson, W_L, associated with the SM $SU(2)_L$ gauge group along with a new (heavy) charged gauge boson, W'_R, associated with the $SU(2)_R$ gauge group. Little Higgs models often introduce an enlarged gauge symmetry that includes new gauge bosons [12]. Other examples are the extradimensional theories in which KK excitations of bulk gauge bosons appear as heavy vector states, such as in the universal extra dimensions [13], in Higgsless models [14], and in warped-space models in which the $SU(2)_R$ is gauged [15] along with the $SU(2)_L$ where the KK gauge bosons may have highly suppressed couplings to the SM light fermions. For the purpose of this work we will not specialize to a specific theory. Instead, we parametrize the chiral coupling in a generic form with a minimal set of parameters.

A. W' Coupling to SM Fermions

We wish to keep this analysis model independent and will parametrize the W' coupling to SM fermions (ψ) using the general form

$$\mathcal{L} = \frac{g_2}{\sqrt{2}} \bar{\psi}_u^i \gamma_\mu \sum_{\tau=L,R} g_\tau V_\tau^{\prime ij} P_\tau \psi_d^j W_\tau^{\prime +\mu} + \text{H.c.,} \quad (2)$$

where (ψ_u, ψ_d) are mass-eigenstate fermions and form a $SU(2)_L$ or $SU(2)_R$ doublet; i, j the generation indices; V' a unitary matrix representing the fermion flavor mixing; and $P_{L,R} = (1 \mp \gamma_5)/2$ the left- and right-chirality projection operators. In our work, we will thus restrict ourselves to renormalizable operators and consider only flavor-diagonal effects, but otherwise will not specialize to any particular model of new physics.

For the sake of convenient comparison with the SM results, we have written the overall coupling strength in terms of the $SU(2)$ coupling g_2 in the SM. Some representative choices are

$$g_{L,R}^{ij} \equiv g_{L,R} V_{L,R}^{\prime ij}, \quad \begin{cases} g_L = 1, & g_R = 0, & \text{pure left-handed gauge boson } W'_L, \\ g_L = 0, & g_R = 1, & \text{pure right-handed gauge boson } W'_R, \\ g_L = g_R = 1, & \text{left-right symmetric gauge boson.} \end{cases} \quad (3)$$

Although for illustrations and plots we consider the same-chirality couplings of the W' to the qq' and to the tb, i.e. either both left-handed or both right-handed as above, our analytical expressions are given in full generality. In some cases, there could be more than one W' state with different g_L and g_R. These states could contribute to the same final state and their amplitudes would have to be added coherently, depending on their mass degeneracy. Indeed, if some of these states are quite close in mass, there could arise

interesting structure in the squared amplitude which could be reflected in the angular correlations. In this work, we will explore only a single W' as the lower-lying state beyond the SM. The techniques we develop here could easily be extended to cases with multiple W' states.

In many models of new physics, the $W'WZ$ coupling arises after electroweak symmetry breaking and is typically suppressed by a heavy-light mixing angle (e.g. Refs. [6,7,14]). This coupling can be written as

$$g_{W'WZ} \sim g_{WWZ}^{SM}\left(\frac{M_W}{M_{W'}}\right)^2, \qquad (4)$$

M_W and $M_{W'}$ are the masses of the SM gauge boson $W^\pm$ and W', respectively. The mixing angle suppression may potentially be overcome due to an enhancement of the heavy W' decay into longitudinally polarized W and Z. For a W' coupling to fermions with SM strength and the $W'WZ$ coupling as in Eq. (4), we estimate that the BR of a 1 TeV W' to SM W and Z is approximately 1.3%. Similarly, the BR of a 1 TeV W' to SM W and Higgs boson is about 2%. We will therefore not consider the decay of a heavy W' into SM gauge bosons, but in a particular new-physics scenario the BR into these modes could be sizable.[1]

In this work, we will mainly focus on heavy charged electroweak states decaying to heavy quarks $W' \rightarrow tb$. As will be seen later, there is a major advantage to consider the heavy fermion final state to determine the W' chiral coupling due to the correlation via the top-quark polarization.

B. Constraints on the W' Mass

Constraints on a new gauge boson of Z' or W' come mainly from direct collider searches, indirect bounds from the precision electroweak observables, and flavor-changing–neutral-current processes. We now summarize the ones relevant to our interests.

(1) Direct searches at the Tevatron:
  (i) Assuming no $W - W'$ mixing, SM-type couplings and the decay channel $W' \rightarrow WZ$ is suppressed, a search in the leptonic decay mode $e\nu$ by the CDF collaboration set a bound of $M_{W'} > 788$ TeV for manifest left-right symmetric model [16]. The D0 collaboration recently obtained a lower bound of $M_{W'} > 1$ TeV [17].
  (ii) With right-handed couplings, the absence of the $t\bar{b}$ signal at CDF gives $M_{W'} > 800$ GeV including the W' leptonic decays, and $M_{W'} > 825$ GeV if leptonic decays are forbidden [18].
(2) Precision electroweak bounds
  (i) A recent global fit to various $SU(2)_1 \times SU(2)_2 \times U(1)_X$ models shows that if the gauge couplings are taken as free parameters, the bound on $M_{W'}$ is typically below 1 TeV while the mass of Z' is above 1.5 TeV [19].
  (ii) Bounds resulting from a fit to precision electroweak observables for generic Z' are found in Ref. [20] to be $M_{Z'}/g_{Z'} \gtrsim 2.7$–6.7 TeV. Similar bounds can be applied for the W' since in typical models the W' mass is related to the Z'

mass by an $O(1)$ factor, although it is conceivable that in certain models the splitting could be larger. For a related discussion on such bounds, see also Ref. [5] and references therein.
(3) Low energy bounds
  (i) Global analysis from muon decays, electron-hadron, neutrino-hadron and neutrino-electron interactions in manifest left-right models give $M_{W'} > 715$–875 GeV, depending on the $W_L - W_R$ mixing [21].
  (ii) Bounds from flavor-changing–neutral-current processes in the minimal left-right symmetric model can be as severe as $M_{W'} > 2$ TeV [22], but quite model dependent. With a certain form of the right-handed quark mixing (Cabibbo-Kobayashi-Maskawa quark-mixing matrix matrix), the bound can be relaxed to about 300 GeV [23]. For left-right models with an extended Higgs sector, the bound can also be relaxed to about 1 TeV depending on the structure of the Higgs sector [24,25].

We thus will primarily study the case $M_{W'} = 1$ TeV for illustration, and will comment on the situation for a heavier one.

III. SIGNAL FOR $W' \rightarrow tb$ AT THE LHC

At the LHC, the dominant parton-level subprocess for a heavy W' production is depicted in Fig. 1, as labeled with the corresponding momenta

$$q'(p_1)\bar{q}(p_2) \rightarrow W'^+ \rightarrow t(k_1)\bar{b}(k_2) \rightarrow W^+(q_2)b(k_3)\bar{b}(k_2)$$
$$\rightarrow \ell^+(k_\ell)\nu(k_\nu)b(k_3)\bar{b}(k_2), \qquad (5)$$

plus its conjugate process of W'^- production with a smaller rate. We wish to identify the signal events with a very energetic charged lepton, two high-energy b quark jets, and large missing energy from the undetected neutrino.
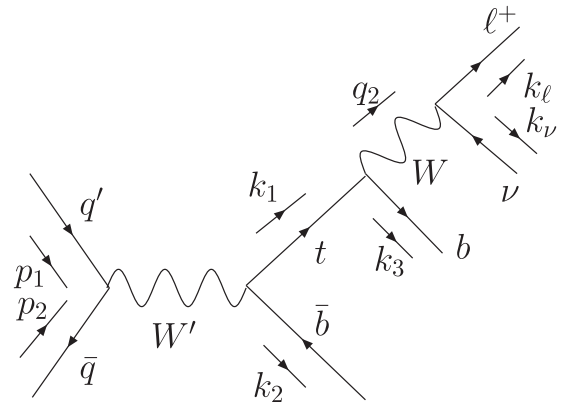

FIG. 1. The partonic level process for a heavy W'^+ production in hadronic collisions.

---

[1]For example in the Randall-Sundrum model in Ref. [6] this coupling is enhanced for longitudinal modes by the volume factor and turns out to be significant.

A. W' Production and Decay

The partial width for W' decaying to a pair of quarks is

$$\Gamma(W' \to \bar{q}q') = 3g_2^2(g_L^{qq'^2} + g_R^{qq'^2})\frac{M_{W'}}{48\pi}, \quad (m_q = m_{\bar{q}} = 0)$$

$$\Gamma(W' \to tb) = 3g_2^2(g_L^{tb^2} + g_R^{tb^2})\frac{M_{W'}}{48\pi}\left(1 - \frac{m_t^2}{M_{W'}^2}\right)$$

$$\times \left(1 - \frac{m_t^2}{2M_{W'}^2} - \frac{m_t^4}{2M_{W'}^4}\right), \quad (m_b = 0). \quad (6)$$

Here and henceforth, we generically denote the W' with both left- and right-handed couplings g_L and g_R, and set the gauge coupling strength to that of the SM $SU(2)$, g_2. The partial widths of the W' to quarks is symmetric under $R \leftrightarrow L$. However, its decay to the leptons will depend upon the lepton spectrum and flavor mixing for a given model. If assuming the SM particle content and no heavy leptons (N, L) below the threshold $M_{W'} < M_L + M_N$, then one only has

$$\Gamma(W'_L \to \ell\nu_i) = g_2^2 g_L^{l\nu^2}\frac{M_{W'}}{48\pi}, \quad (7)$$

where ν_i are the three SM-like light neutrinos. Therefore, the pure gauge eigenstates W'_L and W'_R have different decay widths, given by

$$\Gamma_{W'_R} = \frac{g_2^2 g_R^2 M_{W'}}{16\pi}\left[2 + \left(1 - \frac{m_t^2}{M_{W'}^2}\right)\left(1 - \frac{m_t^2}{2M_{W'}^2} - \frac{m_t^4}{2M_{W'}^4}\right)\right] \quad (8)$$

$$\Gamma_{W'_L} = \frac{g_2^2 g_L^2 M_{W'}}{16\pi}\left[3 + \left(1 - \frac{m_t^2}{M_{W'}^2}\right)\left(1 - \frac{m_t^2}{2M_{W'}^2} - \frac{m_t^4}{2M_{W'}^4}\right)\right]. \quad (9)$$

Figure 2(a) shows the total width of the pure gauge eigenstates $W'_{L,R}$ as a function of $M_{W'}$. The W'_L width is consistently larger than W'_R since it has an additional decay channel to SM leptons, although the partial width for $W' \to t\bar{b}$ is the same for both the left-handed and right-handed cases. Figure 2(b) shows the branching fraction for $W' \to t\bar{b}$ as a function of $M_{W'}$, $\mathrm{BR}(W' \to t\bar{b}) = \Gamma(W' \to t\bar{b})/\Gamma_{W'}$. It is smaller for the left-handed W'.

To calculate the production cross section for the pure gauge eigenstates $W' \to t\bar{b}$ we used the narrow width approximation:

$$\sigma(pp \to W' \to t\bar{b}) \approx \sigma(pp \to W')\mathrm{BR}(W' \to t\bar{b}), \quad (10)$$

where $\sigma(pp \to W')$ is the on-shell production cross section of the W'. Figure 2(c) shows the production cross section for the pure gauge eigenstate W'^+ (solid line) and W'^- (dashed line) before the W' decays, and the cross section for $pp \to W'^+_L \to t\bar{b}$ (dotted line) and $pp \to W'^+_R \to t\bar{b}$ (dash-dotted line) at the 14 TeV LHC, where the cross section is calculated according to Eq. (10). Since the valence quarks of the proton are two u quarks and one d quark, a process with an initial state containing u quarks will have a larger production cross section when compared to a similar process with an initial state containing d quarks. Hence, the W'^+ production cross section is greater than the W'^- production cross section. To be precise, the cross section for W'^+ production ranges from around 2.3 times to 4.2 times larger than the W'^- cross section for a W' mass between 1 and 4 TeV. Also, the cross section for $pp \to W'^+_L \to t\bar{b}$ is smaller than that of $pp \to W'^+_R \to t\bar{b}$ due to the differences in the branching fractions.

The presence of $W'_L \leftrightarrow W'_R$ mixing would alter the above characteristics since the observed mass eigenstate would be a linear combination of the gauge eigenstates W'_L and W'_R. Thus, determining the chiral couplings of the W' state would help in unravelling the presence of such mixings.

B. Event Characteristics and Reconstruction

To determine the W' chiral coupling from angular distributions, one would like to know the charge of the final state particle produced. We thus focus on the leptonic mode of the top-quark decay. The neutrino is unobserved but kinematical constraints can be used to infer its 4-momentum. The transverse momentum of the neutrino can be found by momentum conservation from the observable particles:

$$\mathbf{k}_{\nu T} = -(\mathbf{k}_{\ell T} + \mathbf{k}_{3T} + \mathbf{k}_{2T}) \quad (11)$$

where the momentums are as labeled in Fig. 1, and the subscript T labels the transverse momentum. However, the
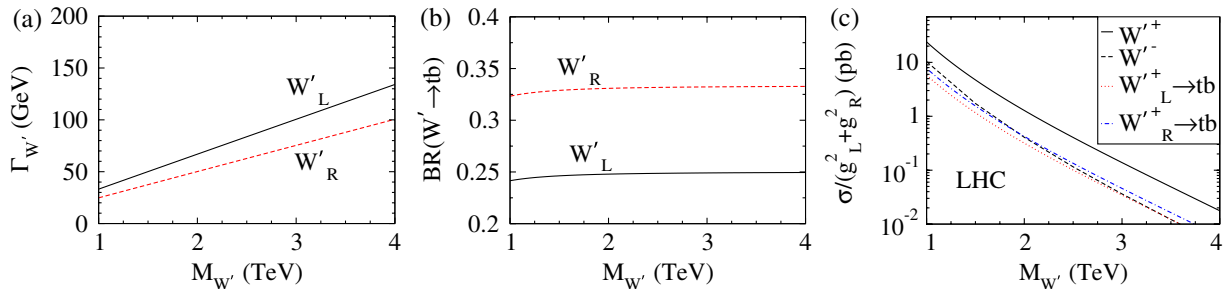

FIG. 2 (color online).   (a) The total decay width, (b) the branching fraction of $W' \to t\bar{b}$, and (c) the cross sections of the production of $W'^\pm$ at the 14 TeV LHC with and without its subsequent decay to $t\bar{b}$, as a function of W' mass for pure gauge eigenstates W'_L and W'_R.

neutrino's longitudinal momentum cannot be determined through momentum conservation due to the unknown boost of the partonic c.m. frame. It can be inferred through the on-shell condition for the W-mass

$$M_W^2 = (k_\nu + k_\ell)^2. \tag{12}$$

Solving this quadratic equation for the neutrino longitudinal momentum leads to a two-fold ambiguity. We further impose the on-shell condition for the top quark

$$m_t^2 = (k_\nu + k_\ell + k_3)^2. \tag{13}$$

In principle, we do not know which of the two b quarks is coming from the top-quark decay. The previous two-fold ambiguity is now a four-fold ambiguity. For each of these four possibilities we evaluate the top mass and pick the solution that is closest to the measured top mass. This resolves the four-fold ambiguity, determines the longitudinal component of the neutrino, and identifies which b quark is the one resulting from top decay. The event can be completely resolved and the $t\bar{b}$ c.m. frame is reconstructed. We have checked against our theoretical calculation that in this method the reconstruction is correct about 99.99% in identifying the b quark, and in identifying the correct neutrino momentum.

Another technique one could use is to assume that the b jet closer (in opening angle) to the lepton is the one from top decay. This is based on the fact that the top quark from a heavy W' decay is rather energetic, so that its decay products are collimated. This method of reconstruction correctly identifies b quark 93.5% of the time and the neutrino momentum 96.7% of the time. We will adopt the first method for the event reconstruction.

Once we have determined the 4-momentum of the neutrino and which b quark results from the top decay, we have fully reconstructed the system and can proceed to form various kinematical quantities which have sensitivity to the W' chiral couplings. In the following calculations, spin correlations in the decay chains have been fully implemented. Let us first examine the transverse momentum distribution for various final state particles. We recall that for a parent particle of mass M decaying to two light particles, the transverse momentum of the final state particle develops a Jacobian peak near $M/2$. This peak will be subsequently smeared by the transverse motion of the parent particle. For the sake of signal illustration in this section, no acceptance cuts are imposed and the SM contribution via W exchange is not included here. In Figs. 3(a) and 3(b), we show the transverse momentum of the two b jets for the W'_L and W'_R, respectively. The harder b jet clearly shows the above kinematical feature from a heavy W' decay. It is interesting to notice the slight difference for the softer b jet in these two panels: W'_L leads to a harder b jet than W'_R. This is a natural consequence of the top-quark spin correlation as illustrated in Fig. 4, where the decay chains of a polarized top quark of L, R helicities are

depicted. Figures. 4(a) and 4(b) illustrate the dominant decay chain with a longitudinally polarized W boson (W_0^+), whereas the accompanying b quark is boosted along (against) its motion by a parent top quark in the case of W'^+_L (W'^+_R). The transverse momentum distributions of the lepton and missing neutrinos for the left-handed [Fig. 3(c)] and right-handed [Fig. 3(d)] W' can be understood similarly as seen in Fig. 4. The charged leptons tend to be softer in the left-handed case than those in the right-handed case, as seen from the correlation in Figs. 4(a) and 4(b). Although subleading with about 30% contribution from the transversely polarized W as shown by Figs. 4(c) and 4(d), the successive boosts of the top and the W in the same (opposite) direction for the W'_L (W'_R) lead to a softer (harder) charged lepton distribution and a harder (softer) E_T distribution as seen in Figs. 3(c) and 3(d). Finally, for the case of W'^+_R, the charged lepton transverse momentum distribution is only slightly harder than that of missing neutrinos, which indicates the slightly larger boost of the top quark in one direction compared to the boost of the W in the opposite direction.

C. Signal Selection and Background Suppression

We perform an analysis including SM contribution

$$pp \rightarrow W^{+*} \rightarrow t\bar{b} \rightarrow \bar{b}b\ell^+\nu, \tag{14}$$

which serves as the irreducible SM background. Interference between the W' and SM diagrams is fully implemented.

To be as realistic as possible, we simulate detector effects by smearing the lepton and jet energies according to the assumed Gaussian resolution parametrization

$$\frac{\sigma(E)}{E} = \frac{a}{\sqrt{E}} \oplus b, \tag{15}$$

where $\sigma(E)/E$ is the energy resolution, a is a sampling term, b is a constant term, $\oplus$ represents addition in quadrature, and all energies are measured in GeV. For leptons we take $a = 5\%$ and $b = 0.55\%$, and for jets we take $a = 100\%$ and $b = 5\%$ [26]. After smearing we apply the basic acceptance cuts:

$$p_T(\ell) > 20 \text{ GeV}, \qquad \eta(\ell) < 2.5,$$
$$p_T(j) > 50 \text{ GeV}, \qquad \eta(j) < 3.0, \tag{16}$$
$$E_T > 25 \text{ GeV}.$$

The angular separation between particle i and particle j is defined by

$$\Delta R_{ij} = \sqrt{\Delta\phi_{ij}^2 + \Delta\eta_{ij}^2}, \tag{17}$$

where $\Delta\phi_{ij}$ is the difference between the particles' azimuthal angles, and $\Delta\eta_{ij}$ is the difference between the particles' rapidities. The top quark and the $\bar{b}$ resulting from the W' will be back-to-back in the transverse plane. Hence, the angular separation between the b resulting from the
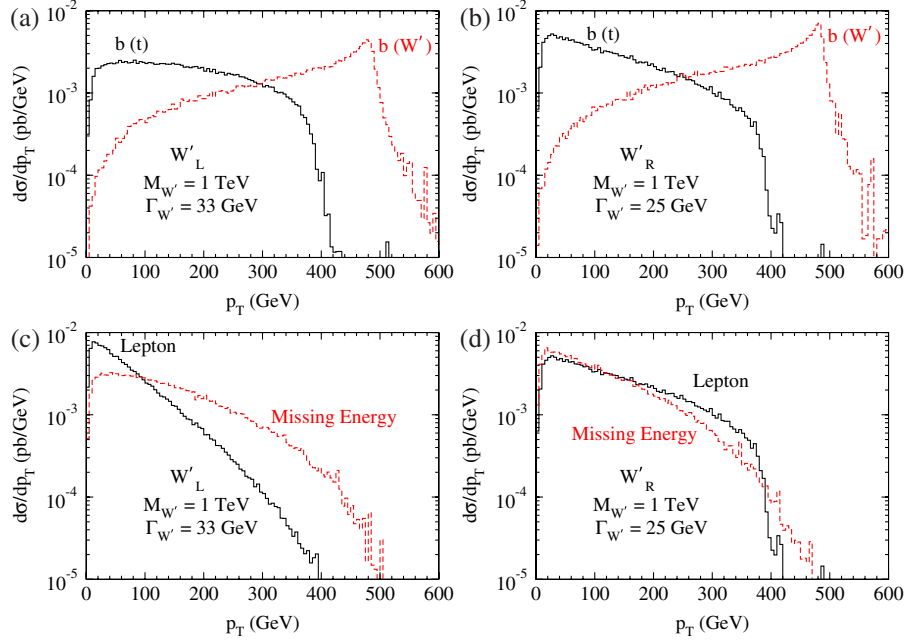
FIG. 3 (color online).   Transverse momentum distributions in $pp \to W' \to t\bar{b} \to b\bar{b}\ell^+ \nu_\ell$ production at the LHC for $M_{W'} = 1$ TeV, for the two b jets from (a) the $W_L'^+$ and (b) $W_R'^+$; and for the lepton and missing energy from (c) the $W_L'^+$ and (d) $W_R'^+$. No acceptance cuts are imposed and the SM W contribution is not included.

top-quark decay and the $\bar{b}$ resulting from the W', ΔR_{bb}, is peaked near π. On the other hand, since the top is highly boosted and its decay products collimated, the angular separation between the lepton and b from the top decay, $\Delta R_{\ell b}$, is peaked at a low value. Hence, a stringent cut on

FIG. 4.   Helicity and spin correlations in the chains $t_{L,R} \to bW^+ \to b\ell^+ \nu_\ell$ from W_L' decay in (a), (c); and from W_R' decay in (b), (d). Figures (a) and (b) are for longitudinally polarized SM W's, and Figs. (c) and (d) are for transversely polarized SM W's. The decay goes from left to right as labeled by the particle names. The momenta (single arrow lines) and spins (double arrow lines) are in the parent rest frame in the direction of the top quark's motion ($\hat{z}$) in the W' rest frame.

$\Delta R_{\ell b}$ would cut out most of our signal. We thus impose the cuts

$$\Delta R_{\ell b} > 0.3, \qquad \Delta R_{bb} > 0.4 \qquad (18)$$

where $\Delta R_{\ell b}$ is the ΔR for the lepton and the b jet resulting from the top decay, and ΔR_{bb} is the ΔR for the two b jets.

Once we have fully reconstructed the event after momentum smearing and including the cuts in Eqs. (16) and (18), we can further reconstruct the partonic c.m. frame, invariant mass $M_{t\bar{b}}$, and the top-quark mass $m_t^{\rm rec}$. The most convincing signal identification would be the reconstruction of the mass peak. Figure 5(a) shows the system invariant-mass distributions for a 1 TeV W_L' and W_R', including the SM contribution. As can be seen, the W_L' and SM W destructively interfere before the resonance peak, while the W_R' and SM W constructively interfere before the peak. Also, near the resonance the W' signal dominates over the SM W. At the W' peak, the small difference between the W_R' and W_L' invariant-mass distributions is due to their different decay widths, resulting in slightly different decay branching fractions to the final states.

As pointed out previously in Ref. [27], since the W_L' (W_R') destructively (constructively) interferes with the SM W before the resonance peak, it may be possible to determine if the W' has left-handed or right-handed couplings by observing the interference region in the total partonic c.m. frame mass distribution. Our proposed observables are defined around the W' resonance peak. Since the interference region has a much lower cross section than the resonance peak, our proposed observables will have a
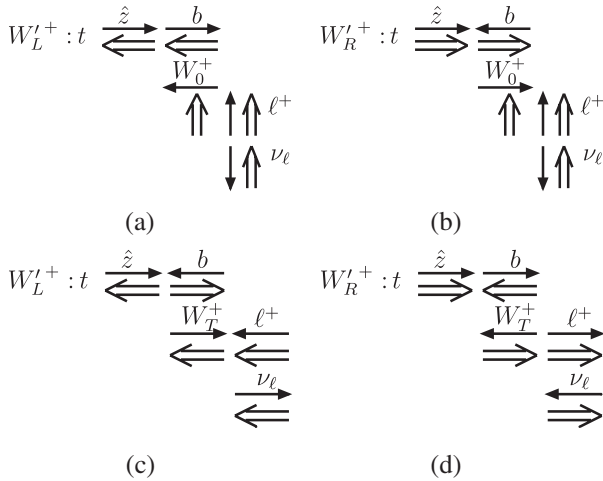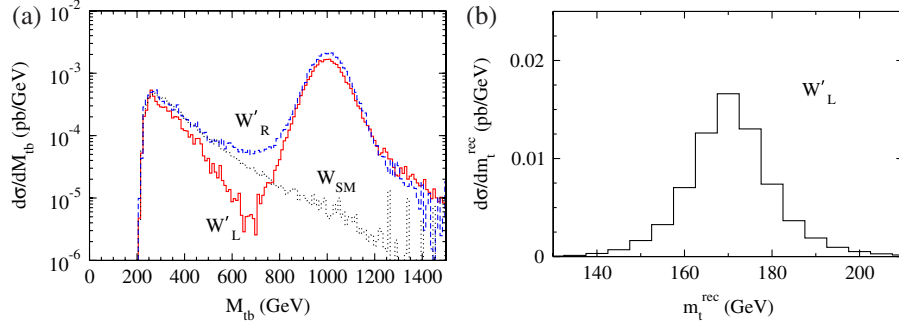
FIG. 5 (color online).   (a) The invariant-mass distribution of tb system for $pp \rightarrow W/W' \rightarrow t\bar{b} \rightarrow b\bar{b}\ell^+\nu$ production at the LHC with $M_{W'} = 1$ TeV with contributions from $W + W'_L$ (solid line), $W + W'_R$ (dashed line), and the standard model W (dotted line); and (b) the invariant-mass distribution for the reconstructed top quark.

better ability to determine the W' chiral couplings once a resonance is observed.

Figure 5(b) shows the reconstructed top mass distribution from a 1 TeV W'_L plus the SM W after momentum smearing, the cuts in Eq. (16), and event reconstruction. The reconstructed top mass distribution stays highly peaked near the measured top mass. The apparent width is dominated by the jet energy resolution. The top-quark reconstructed mass distribution for the W'_R is largely the same.

Motivated by the distributions in Figs. 5(a) and 5(b), we apply cuts on the reconstructed system invariant mass, $M_{t\bar{b}}$, and the reconstructed top-quark mass, m_t^{rec}:

$$M_{W'} - 100 \text{ GeV} \leq M_{t\bar{b}} \leq M_{W'} + 100 \text{ GeV},$$
$$m_t - 20 \text{ GeV} \leq m_t^{\text{rec}} \leq m_t + 20 \text{ GeV}. \qquad (19)$$

In Table I, we show the effects of the cuts on the signal with and without the SM W contribution for a 1 TeV W'. As can be seen, as the cuts progress up to Eq. (19), the SM s channel W background disappears and we are left with our resonance signal.

Besides the SM s channel W background, there is also the irreducible QCD background of $b\bar{b}W^+$. A QCD jet from a light quark or a gluon may be misidentified as a b quark and hence results in reducible backgrounds jjW^+. Furthermore, another large background comes from the t

TABLE I.   Signal cross section $pp \rightarrow t\bar{b} \rightarrow b\bar{b}\ell^+\nu_\ell$ where $\ell = e^+$ or μ^+ for $M_{W'} = 1$ TeV with and without the SM W contribution, with consecutive cuts as listed.

σ (pb)	$W + W'_L$	$W + W'_R$	W'_L	W'_R
No cuts or smearing	1.1	1.4	0.67	0.90
No Cuts	0.92	1.2	0.57	0.75
Cuts Eq. (16)	0.38	0.51	0.32	0.42
+Equation (18)	0.35	0.46	0.30	0.37
+Equation (19)	0.22	0.29	0.22	0.29
+Equation (23) & tagging 1 b jet	0.11	0.16	0.11	0.15
+tagging 2 b jets without Eq. (23)	0.070	0.10	0.070	0.10

channel single top-quark production, $W^* b \rightarrow t$, which can be considered at a more fundamental level as

$$qg \rightarrow q't\bar{b}. \qquad (20)$$

In fact, both q' and $\bar{b}$ in the final state move in the forward direction with a low transverse momentum (at the order of $M_W/2$ and m_b, respectively). If we envision a search for exclusive signal $t\bar{b}$ as Eq. (14), the above backgrounds constitute two classes of final states denoted by $W^+g \rightarrow t\bar{b}$ and $bq \rightarrow tq'$, where q' could fake $\bar{b}$. Hence, in the following analysis we separately consider those two final states and apply no cuts on the additional jet (nor is it used in the reconstruction). Our background estimate is on the conservative side since we could apply an explicit jet-vetoing cut on the extra forward jet in Eq. (20).

The background events are first smeared according to Eq. (15) and then run through the reconstruction algorithm. Although the lepton and neutrino originate from W decay, for some events solving Eq. (12) for the neutrino longitudinal momentum does not result in physical solutions. Analyzing Eq. (12), one can determine that for a solution to exist the following condition must be met:

$$M_W^2 \geq 2k_{\nu T}k_{\ell T}(1 - \cos(\phi_\ell - \phi_\nu)), \qquad (21)$$

where ϕ_i is the azimuthal angle of particle i. If the missing energy and lepton transverse momenta are near $M_W/2$ and nearly back-to-back, once energy smearing is applied it is possible that $4k_{\nu T}k_{\ell T} \geq M_W^2$. Hence, for these events Eq. (21) is not satisfied and there are no physical solutions for the neutrino longitudinal momentum. Events for which solutions do not exist are rejected.

Our background cross sections with consecutive cuts are listed in Table II. As can be seen, after reconstruction and the cuts in Eqs. (16) and (18), the backgrounds still dominate over our signal. Applying the invariant-mass cuts in Eq. (19) suppresses the jjW, tj, Wg backgrounds by 1 to 2 orders of magnitude and the QCD $b\bar{b}W$ background by 3 orders of magnitude while only affecting our signal by 20–30%. Despite the highly effective kinematical cuts, the

TABLE II.   SM background cross sections with consecutive cuts optimized to a 1 TeV W' signal.

σ (pb)	jjW^+	$bq \to tj$	$W^+g \to t\bar{b}$	$b\bar{b}W^+$
Cuts Eqs. (16) and (18)	96	2.3	0.56	0.18
+Equation (19)	1.3	0.080	4.4×10^{-3}	4.6×10^{-4}
+Equation (23) & tagging 1 b jet	2.5×10^{-3}	6.9×10^{-3}	1.5×10^{-3}	2.7×10^{-4}
+tagging 2 b jets without Eq. (23)	1.4×10^{-4}	2.5×10^{-4}	1.6×10^{-3}	1.6×10^{-4}

jjW background cross section is still more than 3 times as large as that of the signal.

To further suppress this background, we consider the b tagging. The probability that a b jet is correctly identified is 60% while the faked rates of mistagging a light jet as a b jet is transverse momentum dependent and we adopt them from [26]:

$$\varepsilon_\ell = \begin{cases} \frac{1}{150} & p_T < 100 \text{ GeV} \\ \frac{1}{450}\left(\frac{p_T}{25 \text{ GeV}} - 1\right) & 100 \text{ GeV} < p_T < 250 \text{ GeV} \\ \frac{1}{50} & p_T > 250 \text{ GeV} \end{cases}$$

(22)

Finally we note, as seen from Figs. 3(a) and 3(b), that the b jet originating from the W' will have a large transverse momentum peaking around $M_{W'}/2$. This highly energetic jet would make the b tagging less efficient and result in a larger fake rate as well. Instead, we could consider to trade this second b tagging for the harder jet with a higher transverse momentum cut

$$p_{T,\text{max}}(j) > 300 \text{ GeV}$$

(23)

The second to last row of Tables I and II shows the effect of the single b tagging plus the cut in Eq. (23) on the harder jet for the signal (background). As can be seen, tagging one b jet and applying an additional p_T cut, Eq. (23), further suppresses the W plus two-jet background by 3 orders of magnitude and the t-channel top-quark background by 1 order of magnitude and only decreases the signal rate by half. For the sake of comparison, the last row of Tables I

and II provides the cross sections obtained from tagging both b jets using the efficiencies above and without the cut in Eq. (23). Tagging both jets as b jets suppresses the Wjj by 4 orders of magnitude and t-channel top-quark backgrounds by 2 orders of magnitude, while the signal rate is decreased, depending on the b tagging efficiency for the high-energy b, by about two thirds. Once the b tagging is implemented, our signal for a 1 TeV W' is larger than the background by at least an order of magnitude.

D. Heavier W' and Highly Boosted Top Quark

The energy of a top quark from the W' decay is roughly $M_{W'}/2$. For a more massive W', the top quark becomes very energetic and its decay products are more collimated. Figure 6(a) shows the ΔR distribution for the lepton and the b jet coming from the top decay and Fig. 6(b) shows the ΔR distribution for the two b jets. Both figures show the distributions for the purely right-handed and the purely left-handed chiral couplings between the SM fermions and a 1 TeV W' after smearing and the cuts in Eq. (16). The lepton and b jet are coming from a boosted top and so should not have much angular separation; hence, the distribution in Fig. 6(a) is peaked at low $\Delta R_{\ell b}$, approximately at $2m_t/E_{tT} \approx 0.5$ for a 1 TeV W'. Since one b jet is coming from the W' decay and the other from the top quark, the two b jets are expected to land on opposite sides of the detector and the distribution in Fig. 6(b) is peaked at large ΔR_{bb} near π.

Let us define an isolated object with a separation cut $\Delta R > 0.3$. Figure 6(c) shows the fraction of events for which the b jet from the top and the lepton can and cannot
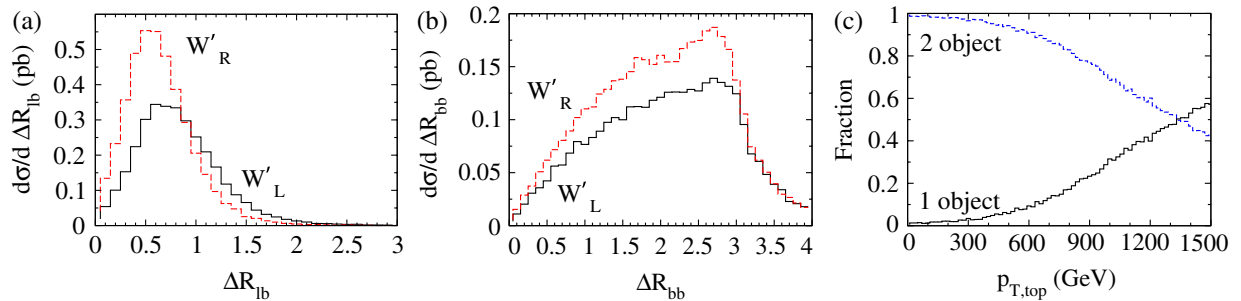

FIG. 6 (color online). $pp \to W' \to t\bar{b} \to b\bar{b}\ell^+\nu_\ell$ production at the LHC for $M_{W'} = 1$ TeV (a) for the distribution $\Delta R_{\ell b}$ between the lepton and the jet identified with the b, (b) for the distribution ΔR_{bb} between the two b jets, and (c) for the fraction of events with the number of objects in the decay of the top quark versus the top transverse momentum.

be resolved with respect to the top transverse momentum. For the sake of illustration, we have used a left-handed W' mass of 3 TeV, although this distribution is largely independent of the W' mass. As the top-quark transverse momentum approaches 1.3 TeV, about one-half of the $b\ell$ events looks like a single object [28], and thus our scheme for the c. m. frame reconstruction is inapplicable. Various methods have been proposed to identify a highly boosted top quark as single "fat top jet" [8,29]. Jet substructures from massive particle decays may help in top-quark identification [30].

IV. W' CHIRAL COUPLINGS FROM ANGULAR CORRELATIONS AT THE LHC

In this section we identify several kinematical quantities that depend directly on the chiral couplings of the W' to SM particles, and show that each has a different dependence on the various chiral couplings of the W' and can be used to determine the couplings.

A. W' Chiral Couplings from Top-Quark Angular Distribution

In the partonic c.m. frame, the polar angular distribution of a final state fermion f via a W' production and decay is given by

$$\frac{d\hat{\sigma}}{d\cos\theta_f}(q\bar{q}' \to W' \to f\bar{f}')$$

$$= \frac{g_2^4}{256\pi}(g_R^{qq'2} + g_L^{qq'2})(g_R^{ff'2} + g_L^{ff'2})$$

$$\times \frac{\hat{s}\lambda^{1/2}(1, x_f^2, x_{f'}^2)}{(\hat{s} - M_{W'}^2)^2 + \Gamma_{W'}^2 M_{W'}^2}\left[1 - (x_f^2 - x_{f'}^2)^2\right.$$

$$- 8x_f x_{f'}\frac{g_R^{ff'}g_L^{ff'}}{g_R^{ff'2} + g_L^{ff'2}} + \lambda(1, x_f^2, x_{f'}^2)\cos^2\theta_f$$

$$\left.+ 2\lambda^{1/2}(1, x_f^2, x_{f'}^2)\frac{g_R^{qq'2} - g_L^{qq'2}}{g_R^{qq'2} + g_L^{qq'2}}\frac{g_R^{ff'2} - g_L^{ff'2}}{g_R^{ff'2} + g_L^{ff'2}}\cos\theta_f\right]$$

$$(24)$$

where $\hat{s}$ is the partonic c. m. energy squared, θ_f the angle between the final-state fermion and the initial-state quark in the c. m. frame, $x_f = m_f/\sqrt{\hat{s}}$, and $\lambda(x, y, z) = (x - y - z)^2 - 4yz$ is the basic two-body kinematic function.

Since the LHC is a pp collider, the quark can come equally from either proton, and a parity-violating angular distribution will be symmetrized, unless we distinguish the direction of the quark from that of the antiquark. This can only be achieved approximately based on the argument that an initial-state quark on average has a higher momentum fraction than an initial-state antiquark, since the former is a valence quark in the proton and the latter a sea quark.

Hence the quark and $W'^{\pm}$ are on average moving in the same direction.

The solid histograms (labeled by "total") in the two panels of Fig. 7(a) show the reconstructed rapidity distribution of the partonic c. m. frame for W'_R and W'_L respectively. In comparison, the dashed histograms (labeled by "correct direction") indicate only those events in which the quark is truly along the W' direction of motion. We see that indeed for $|y_{W'}| > 1.3$, the kinematically reconstructed W' moves mostly along the quark direction. To be more quantitative, Fig. 7(b) shows the fraction of the events the quark and the reconstructed W' are moving in the same direction versus the W' rapidity. Thus, if we apply an appropriate lower bound on the W' reconstructed rapidity (say $y_{W'} > 0.8$), the direction of the quark is mostly in the direction of the W' and hence, the top-quark scattering angle θ_t can be properly defined experimentally. This observation, as proposed and studied earlier in [4], has already been carefully examined in Ref. [31] for neutral current di-lepton events from a heavy Z' at the LHC. In the above treatment, we have imposed the cuts in Eq. (19) to ensure the W' is nearly on-shell. We did not smear the energy nor require a b tagging.

To illustrate the validity of the reconstruction method and the effects of kinematical cuts, Fig. 8 shows the reconstructed top-quark angular distribution with various kinematical cuts and normalizations. The histograms in Figs. 8(a) and 8(b) show the reconstructed angular distribution of the top quark for W'_L and W'_R, respectively, in the reconstructed c.m. frame, with various cuts on the partonic c.m. frame rapidity as listed in the figures and all of the cuts from Eqs. (16), (18), and (19) except the final state particle rapidity cuts in Eq. (16). Each angular distribution has been normalized to one. The dotted curves present the simple form of $(1 + \cos\theta_t)^2$, as expected for a pure (L or R) chiral coupling. If the direction of the quark is misidentified, the top will be identified as going backward (forward) instead of forward (backward) in the partonic c.m. frame. Without the W' rapidity cut (the dash-dotted histograms) misidentification is frequent and populates the backward region in the angular distribution. The solid histograms are with the most stringent W' rapidity cut $|y_{W'}| > 1.7$, which follow the dotted curves most faithfully, indicating the better choice of the quark momentum direction.

Figures 8(c) and 8(d) show the top-quark angular distribution in the reconstructed c.m. frame for the W'_L and W'_R, respectively, with all the cuts from Eqs. (16), (18), (19), and (23) and various cuts on the partonic c.m. frame rapidity as listed in the figures. To illustrate the effects of the additional kinematical cuts, instead of being normalized to one, each angular distribution is now normalized using the cross section that was employed in the normalization of the corresponding angular distribution in Figs. 8(a) and 8(b). Again, the solid histograms are with the most stringent W' rapidity cut and still follow the
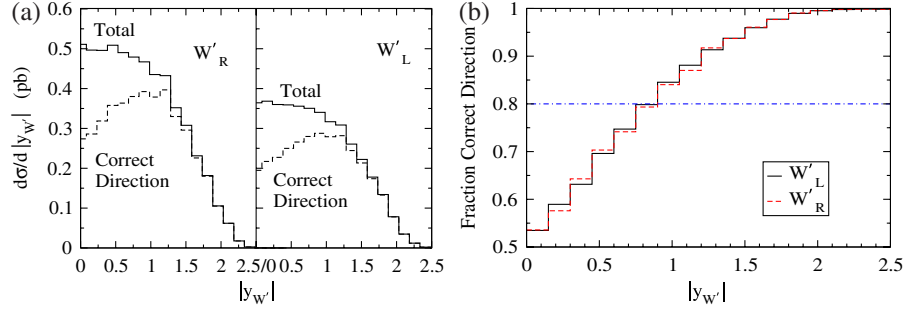
FIG. 7 (color online). $pp \to W' \to t\bar{b} \to b\bar{b}\ell^+ \nu_\ell$ production at the LHC for $M_{W'} = 1$ TeV versus the reconstructed system rapidity $|y_{W'}|$, (a) for all reconstructed events (solid line), and events in which the reconstructed c.m. frame and the quark are moving in the same direction (dashed line, labeled as "correct"), and (b) the event fraction for which the quark is moving in the same direction as the W'.

$(1 + \cos\theta_t)^2$ curve most faithfully for $\cos\theta_t \lesssim 0.25$. For all W' rapidity cuts, the cut of Eq. (23) tends to eliminate events where $\cos\theta_t \approx \pm 1$. The additional deficit or distortion in the high rapidity region for $\cos\theta_t \gtrsim 0.25$ is due to the final-state rapidity cuts of Eq. (16).

This well-known distribution in Fig. 8 can be easily understood based on the argument of spin correlations, as shown in Figs. 9(a) and 9(b), for the W'_L and W'_R cases, respectively. Once again, the single arrow lines represent the particle momenta and the double arrow lines the particle helicities. For our process, the top quark is very energetic and its helicity state largely coincides with a fixed chirality state. A W'_L (W'_R) should couple to left-handed (right-handed) particles and right-handed (left-handed) antiparticles. Since the top-quark spin is

preferentially in the same direction as the spin of the initial-state quark, the top-quark momentum will preferentially be in the same direction as the initial-state quark momentum. This argument works for both the W'_L and the W'_R cases. This feature can be confirmed from our analytical expression in Eq. (24), where the symmetry under $g_L \leftrightarrow g_R$ is evident.

For a more general case, g_L and g_R may be both nonzero and nonequal. The relevant observable to determine chiral couplings is the forward-backward asymmetry, defined by

$$A_{\text{FB}} = \frac{\sigma(\cos\theta_t > 0) - \sigma(\cos\theta_t < 0)}{\sigma(\cos\theta_t > 0) + \sigma(\cos\theta_t < 0)}, \quad (25)$$

which reflects the parity property of the interaction. Using Eq. (24), we find that in the partonic c.m. frame
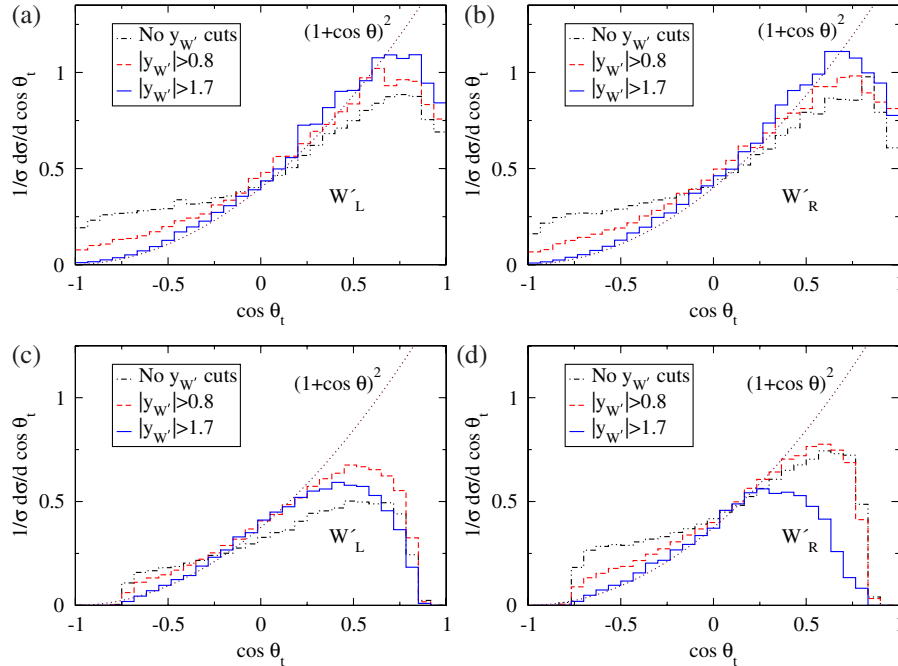

FIG. 8 (color online). The angular distribution of the top quark in the reconstructed c.m. frame in $pp \to W' \to t\bar{b}$ production at the LHC for $M_{W'} = 1$ TeV, with different rapidity cuts, with (a) and (c) for W'_L and (b) and (d) for W'_R.
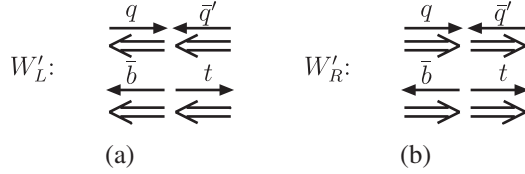
FIG. 9. The helicity and spin correlations between the initial state $q\bar{q}'$ and final state $t\bar{b}$ for (a) and (b) with W'_L and W'_R respectively. The single arrowed lines show the momentum of the particle, and the double arrowed lines show the spin.

$$\hat{A}^{qq'}_{\text{FB}} = \frac{3}{4(1 + x_t^2/2)} \frac{(g_R^{tb2} - g_L^{tb2})}{(g_R^{tb2} + g_L^{tb2})} \frac{(g_R^{qq'2} - g_L^{qq'2})}{(g_R^{qq'2} + g_L^{qq'2})}. \quad (26)$$

Convolving with the parton distribution functions and using the narrow width approximation for the W', the hadronic forward-backward asymmetry is

$$A_{\text{FB}} = \frac{3}{4(1 + x_t^2/2)} \frac{(g_R^{tb2} - g_L^{tb2})}{(g_R^{tb2} + g_L^{tb2})}$$
$$\times \frac{\sum\limits_{qq'}(g_R^{qq'2} - g_L^{qq'2})(q \otimes q')(\tau_0)}{\sum\limits_{qq'}(g_R^{qq'2} + g_L^{qq'2})(q \otimes q')(\tau_0)}, \quad (27)$$

where $\tau_0 = M^2_{W'}/S$, and the $\otimes$ indicates a convolution defined by

$$(q \otimes q')(x) = \int_x^1 \frac{dz}{z} q(z)q'\left(\frac{x}{z}\right). \quad (28)$$

Since the narrow width approximation was used, x_t is now $m_t/M_{W'}$. For a W' mass of 1 TeV and purely left-handed or right-handed couplings to SM fermions, the theoretical value of the partonic and hadronic forward-backward asymmetry is 0.74.

Table III presents the total cross section and the predicted A_{FB} for pure L and R chiral couplings with $M_{W'} = 1$ TeV for various values of cutoff on $y_{W'}$. The other cuts applied are given in Eqs. (16), (18), (19), and (23). As

noted in Eq. (24), forward-backward asymmetry for W'_L and W'_R are largely the same, with the differences due to how the kinematical cuts affect the two cases differently. Also, as the cut on the c.m. frame rapidity increases, reconstructed and true forward-backward asymmetries converge. The forward-backward asymmetry is lowered from the maximum theoretical value because of the reduction in the forward region. As seen explicitly in Eqs. (24), (26), and (27) and demonstrated in this Table, the top-quark angular distribution and forward-backward asymmetry cannot distinguish between the W'_L and W'_R cases. Different values from the prediction in this table may help probe the mixed nature of the chiral couplings.

B. W' Chiral Couplings from Top Spin Correlation with Lepton Angle

The chirality of the W' coupling to SM fermions is best encoded in the polarization of the top quark. Following the arguments presented in [10,32], one may utilize the spin correlation of the top quark. As already discussed, Fig. 4 shows the full spin correlations of the relevant particles in the initial and final states for intuitive understanding. Under the narrow width approximation of the top quark, the production of $t\bar{b}$ and decay $t \rightarrow b\ell^+ \nu_\ell$ can be factorized. We start by considering the polarized top-quark production

$$q'(p_1)\bar{q}(p_2) \rightarrow W' \rightarrow t(k_1, s_t)\bar{b}(k_2), \quad (29)$$

The top spin vector has the properties

$$s_t^2 = -1,$$

$$k_1 \cdot s_t = 0, \quad \text{and} \quad s_t^\mu = \left(\frac{\vec{k}_1 \cdot \hat{s}_t}{m_t}, \hat{s}_t + \frac{\vec{k}_1(\vec{k}_1 \cdot \hat{s}_t)}{m_t(m_t + E_1)}\right), \quad (30)$$

where E_1 and $\vec{k}_1$ are the energy and the 3-momenta of the top quark in the partonic c.m. frame and $\hat{s}_t$ the top spin three-vector in its rest frame. The cross section for the process in Eq. (29) is of the following form

TABLE III. Cross section for $pp \rightarrow W' \rightarrow t\bar{b} \rightarrow b\bar{b}\ell^+ \nu_\ell$ production at the LHC for $M_{W'} = 1$ TeV and forward-backward asymmetry of the top quark in the partonic c.m. frame for various values of cutoff on $y_{W'}$.

σ (fb)	W'_L		W'_R	
$y_{\text{cut}} > 0$	110		150	
0.8	55		78	
1.2	30		42	
1.7	7.6		9.9	
A_{FB}	True kinematics	Reconstructed	True kinematics	Reconstructed
$y_{\text{cut}} > 0$	0.61	0.32	0.61	0.32
0.8	0.59	0.45	0.58	0.45
1.2	0.56	0.49	0.54	0.48
1.7	0.47	0.45	0.40	0.39

$$d\sigma(s_t) = \frac{1}{2\hat{s}}\frac{1}{4}dPS_2|\mathcal{M}|^2, \quad |\mathcal{M}|^2 = \frac{g_2^4}{4}(A_0 + B_\mu s_t^\mu),$$
(31)

where dPS_2 is the 2-particle phase space and $|\mathcal{M}|^2$ is the polarized invariant amplitude squared. We find

$$A_0 = \frac{8}{(\hat{s} - M_{W'}^2)^2 + \Gamma_{W'}^2 M_{W'}^2}\left\{[g_L^{tb^2}g_L^{qq'^2} + g_R^{tb^2}g_R^{qq'^2}]\right.$$
$$\times (k_1 \cdot p_2)(k_2 \cdot p_1) + [g_L^{qq'^2}g_R^{tb^2} + g_L^{tb^2}g_R^{qq'^2}]$$
$$\left.\times (k_1 \cdot p_1)(k_2 \cdot p_2) - \frac{\hat{s}}{2}m_b m_t[g_L^{qq'^2} + g_R^{qq'^2}]g_L^{tb}g_R^{tb}\right\}, \quad (32)$$

$$B_\mu = \frac{8m_t}{(\hat{s} - M_{W'}^2)^2 + \Gamma_{W'}^2 M_{W'}^2}\left\{[g_L^{qq'^2}g_R^{tb^2} - g_L^{tb^2}g_R^{qq'^2}]\right.$$
$$\times (k_2 \cdot p_2)p_{1\mu} - \frac{m_b}{m_t}g_L^{tb}g_R^{tb}(g_L^{qq'^2} - g_R^{qq'^2})$$
$$\times [(k_1 \cdot p_2)p_{1\mu} - (k_1 \cdot p_1)p_{2\mu}]$$
$$\left.+ [g_R^{tb^2}g_R^{qq'^2} - g_L^{tb^2}g_L^{qq'^2}](k_2 \cdot p_1)p_{2\mu}\right\}. \quad (33)$$

The $B_\mu s_t^\mu$ term contains information about whether the W' has purely right-handed or left-handed chiral couplings. By averaging over the top-quark spin we reproduce Eq. (24) but lose the ability to determine whether the W' is right-handed or left-handed. To discriminate between the right-handed and left-handed cases we need an observable that is dependent on the $B_\mu s_t^\mu$ term.

We now consider the polarized top-quark decay. The terms related to $B_\mu s_t^\mu$ will contribute to the spin observables $\langle \hat{s}_t \cdot \hat{a} \rangle$ where $\hat{a}$ is a suitably chosen spin-quantization axis. Obviously, this observable will have different sign for pure left-handed and right-handed interactions. In terms of an angle (θ_ℓ) between the direction of the charged lepton and the direction $\hat{a}$ [33] in the top rest frame, the angular distribution for a polarized top decay can be written as

$$\frac{d\Gamma_{s_t}}{d\cos\theta_\ell} = \frac{1}{2}\sigma\{1 + 2A\cos\theta_\ell\}, \quad (34)$$

where A can be related to an observed forward-backward asymmetry similarly to Eq. (25). While the direction $\hat{a}$ can be chosen freely, different choices can change the magnitude of A, thus called an "analyzing power". The simplest choice of θ_ℓ can be taken to be the angle between the lepton and the b jet. Specifically for the process under consideration, we may take the b jet that is closer to the lepton in the lab frame, since this one is most likely to originate from the top decay. With that choice of $\hat{a}$ one finds that the analyzing power is $A = 0.36(0.35)$ for the W'_L (W'_R), without smearing or cuts, which does not clearly differentiate between the two cases L and R. This is due to the kinematics that the top quark is highly boosted for both W'_L and W'_R, and also due to the relative kinematics between the b and lepton being the same for both the W'_L and W'_R cases as can be inferred from Fig. 4. A similar effect

happens when θ_ℓ is the opening angle between the lepton and the b jet from the W' decay. Hence, we need to reconstruct the system and define a suitable direction $\hat{a}$.

At high energies, a natural choice of $\hat{a}$ is the top-quark 3-momenta direction in the $t\bar{b}$ c.m. frame. Since the top is nearly in a helicity state, $\langle \hat{s}_t \cdot \hat{k}_1 \rangle$ should be large and increase our sensitivity to the chiral couplings. With this choice and using the narrow width approximation for the top quark and W decays, the lepton angular distribution in the top-quark rest frame is

$$\frac{d\hat{\sigma}(q\bar{q}' \to W' \to t\bar{b} \to b\bar{b}\ell\nu)}{d\cos\theta_\ell}$$
$$= \frac{1}{2}\hat{\sigma}_0\left(1 + \frac{g_R^{tb^2} - g_L^{tb^2}}{g_R^{tb^2} + g_L^{tb^2}}\frac{\hat{s} - m_t^2/2}{\hat{s} + m_t^2/2}\cos\theta_\ell\right), \quad (35)$$

where

$$\hat{\sigma}_0 = \frac{g_2^8}{3 \cdot 2^{15}\pi^3}\frac{m_t M_W}{\Gamma_t \Gamma_W}(g_L^{qq'^2} + g_R^{qq'^2})(g_L^{tb^2} + g_R^{tb^2})$$
$$\times (x_{wt}^2 - 1 - \log x_{wt}^2)(1 - x_t^2)^2\left(1 + \frac{x_t^2}{2}\right)$$
$$\times \frac{\hat{s}}{(\hat{s} - M_{W'}^2)^2 + \Gamma_{W'}^2 M_{W'}^2}, \quad (36)$$

with $x_{wt} = M_W/m_t$ and $x_t = m_t/\sqrt{\hat{s}}$. Some technical details of this calculation are given in Appendix A. For an on-shell W', we can read the analyzing power as

$$A = \frac{1}{2}\left(\frac{g_R^{tb^2} - g_L^{tb^2}}{g_R^{tb^2} + g_L^{tb^2}}\right)\left(\frac{M_{W'}^2 - m_t^2/2}{M_{W'}^2 + m_t^2/2}\right). \quad (37)$$

It is evident that A has opposite sign for pure left-handed and pure right-handed cases, and lies between $-1/2$ and $1/2$ for a L-R mixed W'. The observables in Eqs. (35) and (37) are sensitive to how the top is polarized which in turn only depends on $g_{L,R}^{tb}$ and not on $g_{L,R}^{qq'}$; the kinematics of top production, for instance the θ_t distribution discussed in Sec. IVA, however, are sensitive to the latter coupling as well.

Using the reconstructed events as discussed in the previous section, we can find the angular distribution of the lepton in the top rest frame. The results of this reconstruction are shown in Fig. 10 after convolving with the parton distribution functions. We see the distinctive distributions for the L or R chiral couplings from Fig. 10(a). The charged lepton prefers to move against the direction of the top quark in the partonic c.m. frame in the W'_L case; while in the W'_R case the charged lepton prefers to move in the same direction as the top quark as can be seen in the illustration in Fig. 4. We also illustrate the realistic situation with kinematical cuts as in Fig. 10(b). The main effect of the cuts is to flatten out the distributions somewhat. Around $\cos\theta \approx -1$ the lepton becomes soft and fails
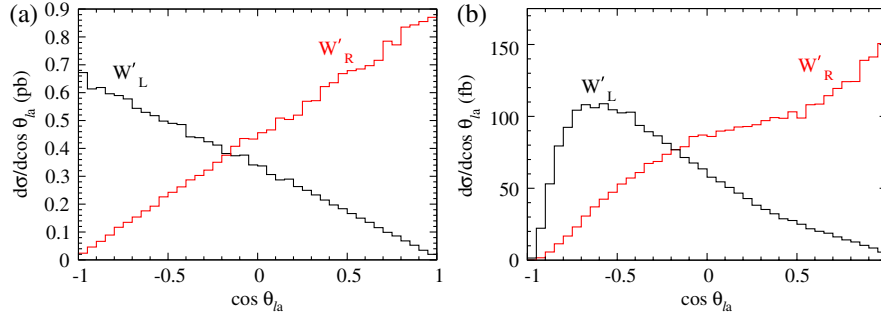
FIG. 10 (color online). The angular distribution of the charged lepton in $pp \to W' \to t\bar{b} \to b\bar{b}\ell^+\nu_\ell$ production at the LHC for $M_{W'} = 1$ TeV in the top-quark rest frame with respect to a spin-quantization direction $\hat{a}$ taken to be the top direction in the c.m. frame, for (a) without smearing or cuts, and (b) with energy smearing and cuts in Eqs. (16), (18), (19), and (23), and tagging the softest b jet.

the transverse momentum cut. Hence the W'_L distribution is affected more by the cuts than the W'_R cut. In spite of the effects of the cuts, we retain an excellent ability to tell W'_L and W'_R apart.

Using the reconstructed events we can also determine the asymmetric observable A. The results for A are given in Table IV for the signal of W'_L and W'_R with and without including the SM W contribution. To demonstrate the realistic kinematical effects, we give the asymmetries with consecutive cuts in the table. Once all the cuts have been applied we still obtain a very good determination of the chirality of the W'.

C. W' Chiral Couplings from Transverse Momentum Distributions

As discussed already in Sec. III B, the p_T distributions also convey information on the W' chirality as shown in Fig. 3 due to their spin correlations. The charged lepton p_T in the case of W'_R is harder than that in W'_L. This can be understood from angular-momentum conservation; for the former the charged lepton moves preferentially in the same direction as the top thereby boosting the lepton p_T, while in the latter it is against this making the lepton p_T softer. The p_T of the b jet from top decay on the other hand has the opposite relationship. Although the W' chirality affects the lepton p_T (and the softer jet p_T), measuring it will require discerning this rather subtle modification which will be limited by statistics.

D. W' Chiral Couplings from other Variables

In this section we explore some other variables that can be used to fix the chirality of the W' couplings.

Because of the spin correlations in the production and decay chain, the W is also polarized in a definite manner. For example, we consider the variable $\cos\theta_{\ell\hat{w}}$, the angle the lepton makes in the W rest frame relative to the direction ($\hat{w}$) of the W in the lab frame with our fully reconstructed events. In Fig. 11 we show its differential distribution for pure left- and right-chiral cases. As can be seen in the figure, we have an ability to determine the W' chirality using this observable, but for a reason not as direct as in the previous subsections. From Fig. 4 we see that the $\cos\theta_\ell$ distribution with respect to the W direction is the same for both W'_L and W'_R, but one has to keep in mind that in this figure the W direction is as seen in the top rest frame. However, the boost of the top plus the selection of the large system rapidity by the $|y_{W'}|$ cut carries the W in the quark direction in the lab frame effectively flipping the W momentum arrow in Fig. 4(d). It then becomes clear why the $\cos\theta_{\ell\hat{w}}$ distribution ends up distinguishing between W'_L and W'_R as seen in Fig. 11. The kinematics we have here ends up being favorable for this variable to differentiate between the chiralities and may not be as general a method as those presented in the previous subsections.

In our work, we have focused on angular correlations of the lepton since it is experimentally clean, but one can consider angular correlations of jet observables also. For

TABLE IV. Forward-backward asymmetry of the charged lepton in $pp \to t\bar{b} \to b\bar{b}\ell^+\nu_\ell$ for $\ell = e^+$ or μ^+ at the LHC for $M_{W'} = 1$ TeV with and without the SM W contribution.

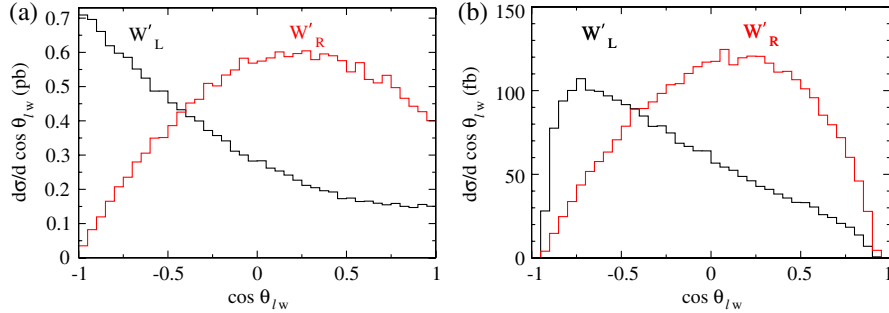| A	$W + W'_L$	$W + W'_R$	W'_L	W'_R
No Cuts or smearing	-0.42	0.17	-0.48	0.48
No Cuts	-0.42	0.15	-0.49	0.45
Cuts Eqs. (16)	-0.48	0.24	-0.51	0.37
+Equation (19)	-0.49	0.39	-0.49	0.40
+Equation (18)	-0.53	0.36	-0.53	0.37
+Equation (23) & tagging 1 b jet	-0.48	0.40	-0.48	0.40

FIG. 11 (color online).   The angular distribution of the charged lepton in $pp \rightarrow W' \rightarrow t\bar{b} \rightarrow b\bar{b}\ell^+ \nu_\ell$ production at the LHC for $M_{W'} = 1$ TeV in the W rest frame with respect to the W moving direction for (a) without smearing or cuts, and (b) with energy smearing and cuts Eqs. (16), (18), (19), and (23), and tagging the softest jet.

instance, the angular distribution with respect to the top direction of the (softer) b jet coming from top decay in the top rest frame also analyzes the top polarization and thus can be used to extract $g_{L,R}^{tb}$. Another example is the angular distribution of the harder b jet with respect to the quark direction which carries the same information as the top angular distribution given in Eq. (24). Rather than analyzing the variables in the top rest frame as we have chosen to do, one can consider observables in the lab frame or with the event partially reconstructed that are sensitive to the chirality as discussed elsewhere [34].

V. DISCUSSION AND CONCLUSIONS

Many beyond the SM theories predict new heavy gauge bosons. If the masses of these new resonant states are not more than a few TeV and their couplings to SM fermions are not too suppressed, the LHC has a good chance of discovering these new resonant states. After discovery, it will become imperative to determine the properties of the new gauge boson, such as spin, mass, and couplings. Of them all, the critically important feature would be their chiral couplings to SM fermions.

In this paper we focused on measuring the chiral couplings between SM fermions and a new heavy, charged gauge boson (W'). Specifically, the chiral couplings of W' t b is determined through the process $pp \rightarrow W' \rightarrow t\bar{b} \rightarrow \ell^+ \nu_\ell b\bar{b}$ by fully reconstructing the event and forming various angular distributions.

We have demonstrated that it is possible to reconstruct the forward-backward asymmetry of the top quark in the partonic c.m. frame. However, this forward-backward asymmetry is unable to distinguish between purely right-handed and purely left-handed chiral couplings. The chiral nature of the W' t b coupling is reflected in the top-quark polarization. A good diagnostic of the top-quark polarization is the forward-backward asymmetry of the lepton. We have shown that by measuring the lepton's forward-backward asymmetry in the top quark's rest frame one can determine the W' t b chiral couplings. Once the W' t b chiral couplings are determined, the top quark's forward-

backward asymmetry in the partonic c.m. frame can be used to determine the chiral couplings of the W' with the initial-state quarks.

The reconstruction method described in this paper is quite general. The procedure to determine the W' chiral couplings to SM fermions described in this paper could be adapted to gauge bosons decaying to new heavy fermions.

APPENDIX A: LEPTON ANGULAR DISTRIBUTION

Here we present details on deriving the lepton angular distribution in the top rest frame. First, the partonic cross section is given by the usual formula

$$d\hat{\sigma} = \frac{1}{2\hat{s}} \frac{1}{4N_C^2} \sum |\mathcal{M}|^2 dPS_4, \qquad (A1)$$

where $N_C = 3$ is the number of colors, the sum is over the external particle spins and colors, $\mathcal{M}$ is the matrix element, and dPS_4 is the four body phase space of the final state lepton, neutrino, and two bottom quarks. Using the narrow width approximation for the top quark and SM W, the sum over the matrix element squared is found to be

$$\sum |\mathcal{M}|^2 = \frac{8N_C^2 g_2^{\,8} \pi^2}{\Gamma_t m_t \Gamma_W M_W} \frac{\delta(k_1^2 - m_t^2)\delta(q_2^2 - M_W^2)}{(\hat{s} - M_{W'}^2)^2 + \Gamma_{W'}^2 M_{W'}^2}$$

$$\times k_3 \cdot k_\nu \{ g_L^{qq'^2} g_L^{tb^2} p_1 \cdot k_2(2p_2 \cdot k_1 k_1 \cdot k_\ell$$

$$- p_2 \cdot k_\ell m_t^2) + g_L^{qq'^2} g_R^{tb^2} p_2 \cdot k_2 p_1 \cdot k_\ell m_t^2$$

$$+ g_R^{qq'^2} g_L^{tb^2} p_2 \cdot k_2(2p_1 \cdot k_1 k_1 \cdot k_\ell - p_1 \cdot k_\ell m_t^2)$$

$$+ g_R^{qq'^2} g_R^{tb^2} p_1 \cdot k_2 p_2 \cdot k_\ell m_t^2 \},$$

where the momenta are as labeled in Fig. 1 and $m_b = 0$. To evaluate the four body phase space we use the phase-space recursion formula:

$$dPS_4 = dPS_2(k_1, k_2)dPS_3(k_3, k_\ell, k_\nu)\frac{dk_1^2}{2\pi}. \qquad (A2)$$

The goal is to obtain the lepton angular distribution in the top quark's rest frame with the z direction defined as the top quark's direction in the partonic c.m. frame. Hence, the matrix element squared needs to be evaluated in the top quark's rest frame. Since the momenta k_1 and k_2 are fixed in the top quark's rest frame, they cannot be integrated over in the phase space $dPS_2(k_1, k_2)$. We will thus evaluate the phase space $dPS_2(k_1, k_2)$ in the partonic c.m. frame and obtain p_1, p_2, k_1, and k_2 in the top quark's rest frame in terms of the top-quark angles in the partonic c.m. frame. The phase space and matrix element squared can be evaluated in two different frames since they are independently Lorentz invariant. Once this procedure is complete, we can integrate the matrix element squared evaluated in the top-quark rest frame over the top-quark angles in the partonic c.m. frame.

First, in the partonic c.m. frame, the 2-body phase space is given by

$$dPS_2(k_1, k_2) = \frac{1 - x_t^2}{2(4\pi)^2} d\cos\theta_1 d\phi_1, \qquad (A3)$$

where $x_t = m_t/\sqrt{\hat{s}}$, θ_1 is the angle the top quark makes with the initial-state quark in the partonic c.m. frame, and ϕ_1 is the top quark's azimuthal angle in the partonic c.m. frame.

To evaluate the momenta in the top quark's rest frame we start with the initial-state quarks, top quark, and antibottom quark momenta in the partonic c.m. frame, rotate the momenta so that the top quark is in the z direction, and boost the system to the top-quark rest frame. These operations take us to the top quark's rest frame with the desired orientation. Assuming that in the partonic c.m. frame the initial-state quark is moving in the z direction and the top-quark momentum is in the y-z plane, the resulting momenta are found to be

$$p_1 = \frac{\hat{s}}{4m_t}(1 - \cos\theta_1 + x_t^2(1 + \cos\theta_1), 0, -2x_t\sin\theta_1,$$

$$- (1 - \cos\theta_1) + x_t^2(1 + \cos\theta_1)),$$

$$p_2 = \frac{\hat{s}}{4m_t}(1 + \cos\theta_1 + x_t^2(1 - \cos\theta_1), 0, 2x_t\sin\theta_1,$$

$$- (1 + \cos\theta_1) + x_t^2(1 - \cos\theta_1)),$$

$$k_1 = (m_t, 0, 0, 0), \quad \text{and} \quad k_2 = \frac{\hat{s}}{2m_t}(1 - x_t^2)(1, 0, 0, -1). \qquad (A4)$$

Substituting these momenta into the matrix element squared and integrating over the 2-body phase space, the differential cross section becomes

$$d\hat{\sigma} = \frac{g_2^{\,8}}{3 \cdot 2^7} \frac{\hat{s}(1 - x_t^2)^2}{\Gamma_t \Gamma_W M_W} \frac{k_3 \cdot k_\nu E_\ell}{(\hat{s} - M_{W'}^2)^2 + \Gamma_{W'}^2 M_{W'}^2}(g_L^{qq'^2}$$

$$+ g_R^{qq'^2})(g_L^{tb^2} + g_R^{tb^2})\Bigg\{(2 + x_t^2)\Bigg[1 + \frac{g_R^{tb^2} - g_L^{tb^2}}{g_R^{tb^2} + g_L^{tb^2}}$$

$$\times \frac{2 - x_t^2}{2 + x_t^2}\cos\theta_\ell\Bigg] + \frac{g_L^{qq'^2} - g_R^{qq'^2}}{g_L^{qq'^2} + g_R^{qq'^2}}$$

$$\times \frac{3}{4}\pi x_t \sin\phi_\ell \sin\theta_\ell\Bigg\}\delta(q_2^2 - M_W^2)dPS_3(k_3, k_\ell, k_\nu),$$

$$(A5)$$

where θ_ℓ is the charged lepton's polar angle in the top quark's rest frame with respect to the top quark's direction in the partonic c.m. frame, ϕ_ℓ is the charged lepton's azimuthal angle in the top quark's rest frame, and E_ℓ is the lepton's energy in the top-quark rest frame.

Now, the 3-body phase space in the top quark's center of mass frame is

$$dPS_3(k_3, k_\ell, k_\nu) = \frac{1}{(4\pi)^5}2E_3dE_3d\cos\theta_3d\phi_3d\cos\theta_\ell d\phi_\ell,$$

$$(A6)$$

where E_3 is the bottom quark's energy, θ_3 (ϕ_3) is the bottom quark's polar (azimuthal) angle in the top-quark rest frame, and the integration over the bottom quark's energy is from 0 to $m_t/2$. The delta function in Eq. (A5) can be rewritten as

$$\delta(q_2^2 - M_W^2) = \frac{1}{2m_t}\delta\Big(E_3 - \frac{m_t}{2}(1 - x_{Wt}^2)\Big), \qquad (A7)$$

where $x_{Wt} = M_W/m_t$. This delta function fixes the bottom quark energy. Using the conservation of energy and momentum, we can also solve for the lepton and neutrino four momenta. The relevant quantities for our calculation are

$$E_\ell = m_t \frac{x_{Wt}^2}{1 + \cos\theta_{3l} + x_{Wt}^2(1 - \cos\theta_{3l})} \qquad (A8)$$

$$k_3 \cdot k_\nu = \frac{m_t^2}{2} \frac{(1 - x_{Wt}^2)(1 + \cos\theta_{3l})}{1 + \cos\theta_{3l} + x_{Wt}^2(1 - \cos\theta_{3l})}, \qquad (A9)$$

where $\cos\theta_{3l} = \sin\theta_\ell \sin\theta_3 \cos(\phi_\ell - \phi_3) + \cos\theta_\ell \cos\theta_3$ is the cosine of the angle between the lepton and the bottom quark.

Using the above identities and integrating over the bottom quark's energy, the lepton angular distribution becomes

$$\frac{d\hat{\sigma}}{d\cos\theta_\ell} = (g_L^{qq'2} + g_R^{qq'2})(g_L^{tb2} + g_R^{tb2})(1 - x_t^2)^2(1 - x_{Wt}^2)^2$$

$$\times \frac{g_2{}^8}{3 \cdot 2^{18}\pi^5} \frac{m_t M_W}{\Gamma_t \Gamma_W} \frac{\hat{s}}{(\hat{s} - M_{W'}^2)^2 + \Gamma_{W'}^2 M_{W'}^2}$$

$$\times \left\{ \left(1 + \frac{x_t^2}{2}\right)\left[1 + \frac{g_R^{tb2} - g_L^{tb2}}{g_R^{tb2} + g_L^{tb2}} \frac{2 - x_t^2}{2 + x_t^2} \cos\theta_\ell\right] \right.$$

$$+ \frac{g_L^{qq'2} - g_R^{qq'2}}{g_L^{qq'2} + g_R^{qq'2}} \frac{3}{8} \pi x_t \sin\phi_\ell \sin\theta_\ell \bigg\}$$

$$\times \frac{1 + \cos\theta_{3l}}{[1 + \cos\theta_{3l} + x_{Wt}^2(1 - \cos\theta_{3l})]^2}$$

$$\times d\cos\theta_3 d\phi_3 d\phi_\ell \qquad (A10)$$

To simplify the integration over the azimuthal angles, we make the variable transformation

$$\phi_+ = \frac{\phi_3 + \phi_\ell}{2}, \qquad \phi_- = \frac{\phi_3 - \phi_\ell}{2}. \qquad (A11)$$

The integration limits for ϕ_- and ϕ_+ are more complicated than the limits for ϕ_ℓ and ϕ_3:

$$\int_0^{2\pi} d\phi_3 \int_0^{2\pi} d\phi_\ell$$

$$= 2\left\{\int_{-\pi}^0 d\phi_- \int_{-\phi_-}^{2\pi+\phi_-} d\phi_+ + \int_0^\pi d\phi_- \int_{\phi_-}^{2\pi-\phi_-} d\phi_+\right\} \qquad (A12)$$

Using the symmetries of the differential cross section to simplify the integration, the lepton angular distribution becomes

$$\frac{d\hat{\sigma}}{d\cos\theta_\ell} = (g_L^{qq'2} + g_R^{qq'2})(g_L^{tb2} + g_R^{tb2})(1 - x_t^2)^2(1 - x_{Wt}^2)^2$$

$$\times \left(1 + \frac{x_t^2}{2}\right)\frac{g_2{}^8}{3 \cdot 2^{15}\pi^3} \frac{m_t M_W}{\Gamma_t \Gamma_W} \frac{\hat{s}}{(\hat{s} - M_{W'}^2)^2 + \Gamma_{W'}^2 M_{W'}^2}$$

$$\times \left[1 + \frac{g_R^{tb2} - g_L^{tb2}}{g_R^{tb2} + g_L^{tb2}} \frac{2 - x_t^2}{2 + x_t^2} \cos\theta_\ell\right] I_1(\cos\theta_\ell),$$

$$\qquad (A13)$$

where

$$I_1(\cos\theta_\ell) = \frac{1}{\pi^2} \int_{-1}^1 d\cos\theta_3 \int_0^\pi d\phi_-(\pi - \phi_-)$$

$$\times \frac{1 + \cos\theta_{3l}}{[1 + \cos\theta_{3l} + x_{Wt}^2(1 - \cos\theta_{3l})]^2}, \qquad (A14)$$

and $\cos\theta_{3l} = \sin\theta_\ell \sin\theta_3 \cos(2\phi_-) + \cos\theta_\ell \cos\theta_3$. To find a solution for I_1, the ϕ_- integral must be analytically continued into the complex plane and a contour integral completed. The details of this calculation are given in Appendix B.

Once I_1 is integrated, we have

$$\frac{d\hat{\sigma}}{d\cos\theta_\ell} = (g_L^{qq'2} + g_R^{qq'2})(g_L^{tb2} + g_R^{tb2})(x_{wt}^2 - 1 - \log x_{wt}^2)$$

$$\times \frac{g_2{}^8}{3 \cdot 2^{16}\pi^3} \frac{m_t M_W}{\Gamma_t \Gamma_W} \frac{\hat{s}}{(\hat{s} - M_{W'}^2)^2 + \Gamma_{W'}^2 M_{W'}^2}$$

$$\times (1 - x_t^2)^2\left(1 + \frac{x_t^2}{2}\right)$$

$$\times \left[1 + \frac{g_R^{tb2} - g_L^{tb2}}{g_R^{tb2} + g_L^{tb2}} \frac{2 - x_t^2}{2 + x_t^2} \cos\theta_\ell\right] \qquad (A15)$$

Hence, at the partonic level, the forward-backward asymmetry of the lepton in the top center of mass frame with the z direction defined as the direction of the top quark in the partonic c.m. frame is

$$\hat{A} = \frac{\hat{\sigma}(\cos\theta_\ell > 0) - \hat{\sigma}(\cos\theta_\ell < 0)}{\hat{\sigma}(\cos\theta_\ell > 0) + \hat{\sigma}(\cos\theta_\ell < 0)}$$

$$= \frac{1}{2}\left(\frac{g_R^{tb2} - g_L^{tb2}}{g_R^{tb2} + g_L^{tb2}}\right)\left(\frac{\hat{s} - m_t^2/2}{\hat{s} + m_t^2/2}\right), \qquad (A16)$$

where

$$\hat{\sigma}(\cos\theta_\ell > 0) = \int_0^1 d\cos\theta_\ell \frac{d\hat{\sigma}}{d\cos\theta_\ell}$$

$$\text{and} \quad \hat{\sigma}(\cos\theta_\ell < 0) = \int_{-1}^0 d\cos\theta_\ell \frac{d\hat{\sigma}}{d\cos\theta_\ell}. \qquad (A17)$$

Assuming the W' is on mass shell, the hadronic forward-backward asymmetry is the same as the partonic forward-backward asymmetry with $\hat{s} = M_{W'}^2$.

APPENDIX B: EVALUATION OF I_1

Here we give the details of how to integrate

$$I_1(\cos\theta_\ell) = \frac{1}{\pi^2} \int_{-1}^1 d\cos\theta_3 I_{\phi_-}(\cos\theta_3, \cos\theta_\ell) \quad (B1)$$

where

$$I_{\phi_-}(\cos\theta_3, \cos\theta_\ell) = \int_0^\pi d\phi_-(\pi - \phi_-)$$

$$\times \frac{1 + \cos\theta_{3l}}{[1 + \cos\theta_{3l} + x_{Wt}^2(1 - \cos\theta_{3l})]^2} \qquad (B2)$$

First, through a change of variable, $\phi' = 2(\pi - \phi_-)$, we can rewrite I_{ϕ_-} as

$$I_{\phi_-}(\cos\theta_3, \cos\theta_\ell) = \frac{1}{4}\int_0^{2\pi} d\phi'\phi'\frac{C + B\cos\phi'}{(F + D\cos\phi')^2},$$

(B3)

where

$$C = 1 + \cos\theta_\ell \cos\theta_3,$$

$$B = \sin\theta_3 \sin\theta_\ell,$$

$$F = 1 + x_{Wt}^2 + (1 - x_{Wt}^2)\cos\theta_\ell \cos\theta_3,$$

$$\text{and} \quad D = (1 - x_{Wt}^2)\sin\theta_\ell \sin\theta_3.$$

(B4)

To compute I_{ϕ_-}, we will consider the contour integral

$$I_C = \oint_C dz \log z \frac{2Cz + B(z^2 + 1)}{(Dz^2 + 2Fz + D)^2},$$

(B5)

where the contour C is illustrated in Fig. 12. We have defined the branch cut of the complex logarithm to be along the positive real axis and deformed the contour about this branch cut. The contour is then a closed loop that consists of these segments:

Segment 1: an arc of a unit circle running for $1 + i\epsilon$ to $1 - i\epsilon$

Segment 2: a straight line from $1 - i\epsilon$ to $-i\epsilon$

Segment 3: half circle of radius ϵ centered about zero running from $-i\epsilon$ to $i\epsilon$

Segment 4: a straight line from $i\epsilon$ to $1 + i\epsilon$

As we will show, Segment 1 is proportional to the integral I_{ϕ_-}.

Using Cauchy's integral formula we can relate the contour integral I_C to the residues of the integrand at the integrand's poles. The integrand in Eq. (B5) has two poles at

$$z_0 = \frac{-F + \sqrt{F^2 - D^2}}{D} \quad \text{and} \quad z_1 = \frac{-F - \sqrt{F^2 - D^2}}{D}.$$
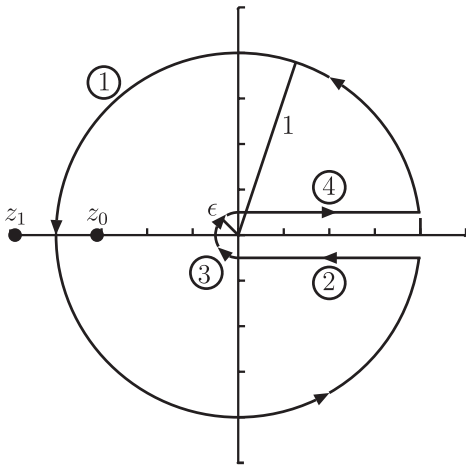
(B6)

FIG. 12. Contour integral for the lepton angular distribution calculation. The points z_0 and z_1 are the poles of the integrand in Eq. (B5).

Since $F > D$, the pole z_0 (z_1) lies on the negative real axis inside (outside) the unit circle centered about zero. These poles are shown in Fig. 12. As can be seen, z_0 is the only pole inside the contour C, and we can use the Cauchy integral formula to find

$$I_C = 2\pi i \text{Res}_{z=z_0} \log z \frac{2Cz + B(z^2 + 1)}{(Dz^2 + 2Fz + D)^2}$$

$$= i\pi \frac{(CD - BF)\sqrt{F^2 - D^2} - D(BD - CF)\log(z_0)}{D(F^2 - D^2)^{3/2}}$$

(B7)

Now the contour will be integrated along all four segments and the limit $\epsilon \to 0$ will be taken. Segment 1 is parametrized by $z = e^{i\phi}$ and ϕ is integrated from ϵ to $2\pi - \epsilon$:

$$I_1 = -\lim_{\epsilon\to 0}\frac{1}{2}\int_\epsilon^{2\pi-\epsilon} d\phi \frac{C + B\cos\phi}{(F + D\cos\phi)^2} = -2I_{\phi_-} \quad \text{(B8)}$$

As mentioned earlier, I_1 is proportional to I_{ϕ_-}.

The parametrization of Segment 2 is $z = x - i\epsilon$ and x is integrated from 1 to 0:

$$I_2 = \lim_{\epsilon\to 0}\int_1^0 dx \log(x - i\epsilon)$$

$$\times \frac{2C(x - i\epsilon) + B((x - i\epsilon)^2 + 1)}{(2F(x - i\epsilon) + D((x - i\epsilon)^2 + 1))^2}$$

(B9)

Since limits of the integral do not depend on ϵ and the integrand is well behaved as $\epsilon \to 0$, we can compute the $\epsilon \to 0$ limit of the integrand and then integrate. The limit of $\log(x - i\epsilon)$ as ϵ goes to zero must be taken carefully. Since the limit as $\epsilon \to 0$ approaches the positive real axis from below, we have

$$\lim_{\epsilon\to 0} \log(x - i\epsilon) = \log|x| + i\lim_{\epsilon\to 0} \arctan\frac{-\epsilon}{x}$$

$$= \log x + 2i\pi,$$

(B10)

Then I_2 becomes

$$I_2 = -\int_0^1 dx \log x \frac{2Cx + B(x^2 + 1)}{(2Fx + D(x^2 + 1))^2}$$

$$- 2i\pi \int_0^1 dx \frac{2Cx + B(x^2 + 1)}{(2Fx + D(x^2 + 1))^2}.$$

(B11)

The second integral in Eq. (B11) can be performed analytically to find

$$-2i\pi \int_0^1 dx \frac{2Cx + B(x^2 + 1)}{(2Fx + D(x^2 + 1))^2}$$

$$= i\pi \frac{(CD - BF)\sqrt{F^2 - D^2} - D(BD - CF)\log(-z_0)}{D(F^2 - D^2)^{3/2}}$$

$$= I_C + \pi^2 \frac{CF - BD}{(F^2 - D^2)^{3/2}},$$

(B12)

where Eq. (B7) has been used to express the integral in terms of I_C. Finally, the integral along Segment 2 is

$$I_2 = - \int_0^1 dx \log x \frac{2Cx + B(x^2 + 1)}{(2Fx + D(x^2 + 1))^2}$$
$$+ I_C + \pi^2 \frac{CF - BD}{(F^2 - D^2)^{3/2}} \tag{B13}$$

For Segment 3 we set $z = \epsilon e^{i\phi}$ and integrate ϕ from $3\pi/2$ to $\pi/2$. The integral is then

$$I_3 = \lim_{\epsilon \to 0} \Bigg\{ -\epsilon \int_{3\pi/2}^{\pi/2} d\phi e^{i\phi} \phi \frac{2C\epsilon e^{i\phi} + B(\epsilon^2 e^{2i\phi} + 1)}{(D\epsilon^2 e^{2i\phi} + 2F\epsilon e^{i\phi} + D)^2}$$
$$+ i\epsilon \log\epsilon \int_{3\pi/2}^{\pi/2} d\phi e^{i\phi} \frac{2C\epsilon e^{i\phi} + B(\epsilon^2 e^{2i\phi} + 1)}{(D\epsilon^2 e^{2i\phi} + 2F\epsilon e^{i\phi} + D)^2} \Bigg\},$$
$$\tag{B14}$$

As ϵ goes to zero, both the integrals in Eq. (B14) are finite and their coefficients go to zero. Hence,

$$I_3 = 0 \tag{B15}$$

Segment 4 is the final segment to be integrated. This segment is parametrized by $z = x + i\epsilon$ and x is integrated from 0 to 1. The integral is then

$$I_4 = \lim_{\epsilon \to 0} \int_0^1 dx \log(x + i\epsilon) \frac{2C(x + i\epsilon) + B((x + i\epsilon)^2 + 1)}{(2F(x + i\epsilon) + D((x + i\epsilon)^2 + 1))^2}$$
$$= \int_0^1 dx \log x \frac{2Cx + B(x^2 + 1)}{(2Fx + D(x^2 + 1))^2}. \tag{B16}$$

As discussed for Segment 2, the integral and ϵ limit can be computed separately since the limits of the integral do not depend on ϵ and the integrand is well behaved in the $\epsilon \to 0$ limit. Also, unlike Segment 2, the positive real axis is approached from above. Hence, the log does not pick up the angle $2i\pi$ that was found for I_2.

Now we are ready to calculate the total contour integral. This is accomplished by adding all four segments together:

$$I_C = I_1 + I_2 + I_3 + I_4 = I_C + \pi^2 \frac{CF - BD}{(F^2 - D^2)^{3/2}} - 2I_{\phi_-}. \tag{B17}$$

Hence, I_{ϕ_-} is found to be

$$I_{\phi_-} = \frac{\pi^2}{2} \frac{CF - BD}{(F^2 - D^2)^{3/2}} \tag{B18}$$

Finally, using the definitions of C, B, F, and D in Eq. (B4) and integrating over $\cos\theta_3$, we can compute

$$\mathcal{I}_1(\cos\theta_\ell) = \frac{x_{wt}^2 - 1 - \log x_{wt}^2}{2(1 - x_{wt}^2)^2}. \tag{B19}$$

---

[1] ATLAS Collaboration, Technical Design Report, Vol. II, ATLAS TDR 14, Report No. CERN/LHCC 99-14.
[2] CMS Collaboration J. Phys. G 34, 995 (2006).
[3] J. C. Pati and A. Salam, Phys. Rev. D **10**, 275 (1974); **11**, 703(E) (1975); G. Senjanovic and R. N. Mohapatra, Phys. Rev. D **12**, 1502 (1975).
[4] P. Langacker, R. W. Robinett, and J. L. Rosner, Phys. Rev. D **30**, 1470 (1984); M. Dittmar, A. S. Nicollerat, and A. Djouadi, Phys. Lett. B **583**, 111 (2004); M. S. Carena, A. Daleo, B. A. Dobrescu, and T. M. P. Tait, Phys. Rev. D **70**, 093009 (2004); T. Han, H. E. Logan, and L. T. Wang, J. High Energy Phys. 01 (2006) 099; F. Petriello and S. Quackenbush, Phys. Rev. D **77**, 115004 (2008).
[5] M. Cvetic, P. Langacker, and J. Liu, Phys. Rev. D **49**, 2405 (1994).
[6] K. Agashe et al., Phys. Rev. D **76**, 115015 (2007).
[7] K. Agashe, S. Gopalakrishna, T. Han, G. Y. Huang, and A. Soni, Phys. Rev. D **80**, 075007 (2009).
[8] K. Agashe, A. Belyaev, T. Krupovnickas, G. Perez, and J. Virzi, Phys. Rev. D **77**, 015003 (2008); A. Djouadi, G. Moreau, and R. K. Singh, Nucl. Phys. **B797**, 1 (2008).
[9] E. Boos, V. Bunichev, L. Dudko, and M. Perfilov, Phys. Lett. B **655**, 245 (2007).
[10] J. M. Frere and W. W. Repko, Phys. Lett. B **254**, 485 (1991).
[11] B. Grzadkowski and Z. Hioki, Phys. Lett. B **476**, 87 (2000); S. D. Rindani, Pramana J. Phys. **54**, 791 (2000); B. Grzadkowski and Z. Hioki, Phys. Lett. B **557**, 55 (2003); R. M. Godbole, S. D. Rindani, and R. K. Singh, J. High Energy Phys. 12 (2006) 021; R. M. Godbole, S. D. Rindani, K. Rao, and R. K. Singh, in SUSY09: 7th International Conference on Supersymmetry and the Unification of Fundamental Interactions, edited by George Alverson, Pran Nath, and Brent Nelson, AIP Conf. Proc. No. 1200 (AIP, New York, 2010).
[12] N. Arkani-Hamed, A. G. Cohen, E. Katz, and A. E. Nelson, J. High Energy Phys. 07 (2002) 034; D. E. Kaplan and M. Schmaltz, J. High Energy Phys. 10 (2003) 039; T. Han, H. E. Logan, B. McElrath, and L. T. Wang, Phys. Rev. D **67**, 095004 (2003).
[13] T. Appelquist, H. C. Cheng, and B. A. Dobrescu, Phys. Rev. D **64**, 035002 (2001); H. C. Cheng, K. T. Matchev, and M. Schmaltz, Phys. Rev. D **66**, 056006 (2002).
[14] C. Csaki, C. Grojean, L. Pilo, and J. Terning, Phys. Rev. Lett. **92**, 101802 (2004); R. S. Chivukula, B. Coleppa, S. Di Chiara, E. H. Simmons, H. J. He, M. Kurachi, and M. Tanabashi, Phys. Rev. D **74**, 075011 (2006); H. J. He et al., Phys. Rev. D **78**, 031701 (2008).

[15] K. Agashe, A. Delgado, M. J. May, and R. Sundrum, J. High Energy Phys. 08 (2003) 050.

[16] A. Abulencia *et al.* (CDF Collaboration), Phys. Rev. D **75**, 091101 (2007).

[17] V. M. Abazov *et al.* (D0 Collaboration), Phys. Rev. Lett. **100**, 031804 (2008).

[18] T. Aaltonen *et al.* (CDF Collaboration), Phys. Rev. Lett. **103**, 041801 (2009).

[19] K. Hsieh, K. Schmitz, J. H. Yu, and C. P. Yuan, Phys. Rev. D **82**, 035011 (2010).

[20] G. Cacciapaglia, C. Csaki, G. Marandella, and A. Strumia, Phys. Rev. D **74**, 033011 (2006).

[21] M. Czakon, J. Gluza, and M. Zralek, Phys. Lett. B **458**, 355 (1999).

[22] G. Beall, M. Bander, and A. Soni, Phys. Rev. Lett. **48**, 848 (1982); G. Ecker and W. Grimus, Nucl. Phys. **B258**, 328 (1985); Y. Zhang, H. An, X. Ji, and R. N. Mohapatra, Phys. Rev. D **76**, 091301 (2007); A. Maiezza, M. Nemevsek, F. Nesti, and G. Senjanovic, Phys. Rev. D **82**, 055022 (2010).

[23] P. Langacker and S. U. Sankar, Phys. Rev. D **40**, 1569 (1989).

[24] Y. L. Wu and Y. F. Zhou, Sci. China, Ser. G: Phys., Mech. Astron. **51**, 1808 (2008); Int. J. Mod. Phys. A **23**, 3304 (2008).

[25] D. Guadagnoli and R. N. Mohapatra, arXiv:1008.1074.

[26] G. L. Bayatian *et al.* (CMS Collaboration), J. Phys. G **34**, 995 (2007); G. Aad *et al.* (The ATLAS Collaboration), arXiv:0901.0512.

[27] T. G. Rizzo, J. High Energy Phys. 05 (2007) 037.

[28] V. Barger, T. Han, and D. G. E. Walker, Phys. Rev. Lett. **100**, 031801 (2008).

[29] D. E. Kaplan, K. Rehermann, M. D. Schwartz, and B. Tweedie, Phys. Rev. Lett. **101**, 142001 (2008); J. Thaler and L.-T. Wang, J. High Energy Phys. 07 (2008) 092.

[30] L. G. Almeida, S. J. Lee, G. Perez, G. F. Sterman, I. Sung, and J. Virzi, Phys. Rev. D **79**, 074017 (2009); L. G. Almeida, S. J. Lee, G. Perez, I. Sung, and J. Virzi, Phys. Rev. D **79**, 074012 (2009).

[31] M. Dittmar, Phys. Rev. D **55**, 161 (1997).

[32] T. M. P. Tait and C. P. P. Yuan, Phys. Rev. D **63**, 014018 (2000).

[33] W. Bernreuther, A. Brandenburg, Z. G. Si, and P. Uwer, Phys. Rev. Lett. **87**, 242002 (2001); Nucl. Phys. **B690**, 81 (2004); W. Bernreuther and Z. G. Si, Nucl. Phys. **B837** 90 (2010).

[34] J. Shelton, Phys. Rev. D **79**, 014032 (2009); D. Krohn, J. Shelton, and L. T. Wang, J. High Energy Phys. 07 (2010) 041.